ACS APPLIED MATERIALS & INTERFACES

Research Article

www.acsami.org

Role of Surface Functionality in the Electrochemical Performance of Silicon Nanowire Anodes for Rechargeable Lithium Batteries

Hui Zhou,[†] Jagjit Nanda,*[,†] Surendra K. Martha,[†,§] Raymond R. Unocic,[†] Harry M. Meyer, III,[†] Yudhisthira Sahoo,*[,‡] Pawel Miskiewicz,[‡,⊥] and Thomas F. Albrecht[‡,∥]

[†]Materials Science and Technology Division, Oak Ridge National Laboratory, Oak Ridge, Tennessee 37831, United States

[‡]Performance Materials & Advanced Technologies, EMD Chemicals, Waltham, Massachusetts 02451-1102, United States

Supporting Information

ABSTRACT: We report the synthesis of silicon nanowires using the supercritical–fluid–liquid–solid growth method from two silicon precursors, monophenylsilane and trisilane. The nanowires were synthesized at least on a gram scale at a pilot scale facility, and various surface modification methods were developed to optimize the electrochemical performance. The observed electrochemical performance of the silicon nanowires was clearly dependent on the origination of the surface functional group, either from the residual precursor or from surface modifications. On the basis of detailed electron microscopy, X-ray photoelectron spectroscopy, and confocal Raman spectroscopy studies, we analyzed the surface chemical reactivity of the silicon nanowires with respect to their electrochemical performance in terms of their capacity retention over continuous charge–discharge cycles.

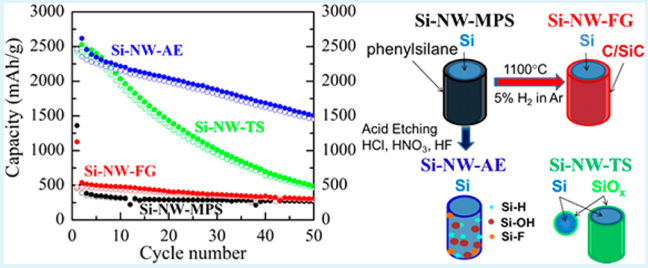

KEYWORDS: *lithium-ion batteries, silicon, nanowire, anode, surface functionality, electrochemistry*

INTRODUCTION

Silicon is one of the most promising anode materials for lithium-ion batteries, because of a number of advantages. Significant among them are its abundance in the earth's crust, its nontoxicity, and a specific capacity that is 1 order of magnitude higher than that of the current state-of-the-art anode for lithium ion, carbon. Such a large increase in capacity is due to the fact that each Si atom can undergo an alloy reaction with 3.75 lithium atoms at room temperature, yielding a capacity close to 4000 mAh/g.[1−3] Further, silicon has an electrochemical potential plateau that is only 100 mV higher than that of carbon, making it a very good candidate to be coupled with high-energy (voltage) cathode materials for achieving a high energy density.[4−6] There have been a number of recent studies demonstrating high reversible capacity and cycle life from electrodes comprising silicon–carbon composites, nanowires, and other forms. However, silicon still suffers from a number of materials and interfacial challenges. The major issues involve (i) an enormous change in volume (>300%) during the lithiation and delithiation, leading to high internal stress that results in electrode pulverization, poor reversibility, and capacity loss,[1,7−10] and (ii) the lack of a mechanistic understanding of the nature of solid electrolyte interphase (SEI) formation on the silicon surface and its stability during the repeated expansion and contraction. The materials and interfacial issues discussed above lead to a significantly higher first-cycle irreversible capacity loss (ICL) and overall lower columbic efficiency.[11−13]

Moving from bulk to nanoscale morphologies affords a promising means of overcoming the first issue, namely the changes in volume associated with lithiation and delithiation. Nanosizing leads to small diffusion length and facile strain relaxation during the lithitation (delithiation) compared to the case in the bulk crystalline phase.[14−18] A variety of silicon nanostructures have been investigated to solve this issue and optimize the cycle life performance. Significant improvements to this effect have been reported in recent literature reports.[6,19−24] As mentioned above, nanostructured Si helps to mitigate the volume expansion aspect, but it introduces some challenges, as well. While the high surface-to-volume ratio can facilitate the diffusion of Li ion and smooth the material stress (strain), it also opens up the potential for uncontrolled and adventitious reactions caused by any moieties on the surface that in principle could affect the electrochemical stability of the silicon electrodes.[25−29]

This study investigates the use of four different types of Si nanowires (NWs) as anode materials. The goal is not the optimization of the electrochemical performance and cycle life of silicon as an anode for lithium batteries but rather to understand the implication of the surface chemistry and functionality of silicon nanowires (NWs) on their electrochemical performance. Another novel aspect of our work is

Received: February 13, 2014
Accepted: April 14, 2014
Published: April 14, 2014

   dx.doi.org/10.1021/am500855a | ACS Appl. Mater. Interfaces 2014, 6, 7607−7614

unlike most reported work on silicon nanostructures that are synthesized and tested at a laboratory scale, our work reports Si-NW samples synthesized and surface treated at a small pilot scale facility leading to a yield of at least gram quantities per batch. Si nanowires (Si-NWs) are synthesized using the supercritical−fluid−liquid−solid (SFLS) growth method, which results in a higher product yield at a relatively low cost.[30−32] The process is called supercritical because the temperature and pressure applied to the closed metallic reactor into which the precursor is passed are well above the critical limits of the solvent toluene. Our study reports the electrochemical performance of Si-NWs synthesized from different precursors as well as under different surface treatment conditions. In each case, we have characterized the surface chemistry of Si-NWs correlated to their observed electrochemical performance. This study reports the electrochemical performance of four different Si-NW samples having distinct surface functionality created by the variation in synthesis conditions and/or postsynthesis processes. Further, to understand the surface chemistry aspect specific to the Si-NWs alone, we do not use any polymeric binders or carbon additives. The Si-NW electrodes are prepared by pressing the Si-NW powders on copper current collectors.

Briefly, we discuss the performance of four types of Si-NWs obtained from two kinds of silicon precursors, phenylsilane and trisilane. Depending on the synthetic process and modification, we noticed varied degrees of electrochemical performance from the Si-NWs depending on their surface chemical groups. Electron microscopy, confocal Raman spectroscopy, and X-ray photoelectron spectroscopy analysis of the Si-NWs reveal the presence of different surface chemical moieties depending on the synthesis method and surface modification. These constitute (i) a phenylsilane-derived shell having Si−H- and Si−C-terminated groups, (ii) carbonaceous and Si−C groups, and (iii) mainly Si−O-type functionality in the case of acid-etched Si-NWs. The impact of various surface termination groups on their electrochemical performance is further discussed for each kind of Si-NW.

EXPERIMENTAL SECTION

Synthesis and Surface Modification of Silicon Nanowires. This work investigates Si-NWs synthesized from two precursors, monophenylsilane (MPS) and trisilane (TS). From MPS, the Si-NWs were synthesized by Au nanocrystal-seeded SFLS growth in toluene with the method reported in ref 32. Briefly, MPS was mixed together with Au nanoparticles (NPs) at a Si:Au molar ratio of 600:1 and diluted with anhydrous toluene to achieve an MPS concentration of 200 mM. Then the nanowires were grown in a preheated sealed titanium reactor at 410 °C and 1200 psi and collected during the semi-continuous flow process.

From the TS precursor, the Si-NWs were synthesized by a process reported previously.[31] In a typical experiment, 200 mg of Au NPs and 100 μL of TS (Si:Au ratio of 45) were added to toluene (volume of 4.5 mL) and introduced into a titanium reactor heated to 430 °C at a rate of 3 mL/min. The product consisted of a mixture of NWs and NPs (<50% NWs). A large fraction of the NPs are due to the uncontrolled or fast reaction kinetics of the TS precursor decomposition. However, this modification leads to another kind of surface chemistry that forms the basis of our study. On the basis of the synthesis and postsynthesis processes, the samples are named as follows (schematic figures shown in Figure 1).

(1) Si-NW-MPS, pristine Si nanowires were synthesized by the procedure described above with the monophenylsilane (MPS) precursor without any further treatments.

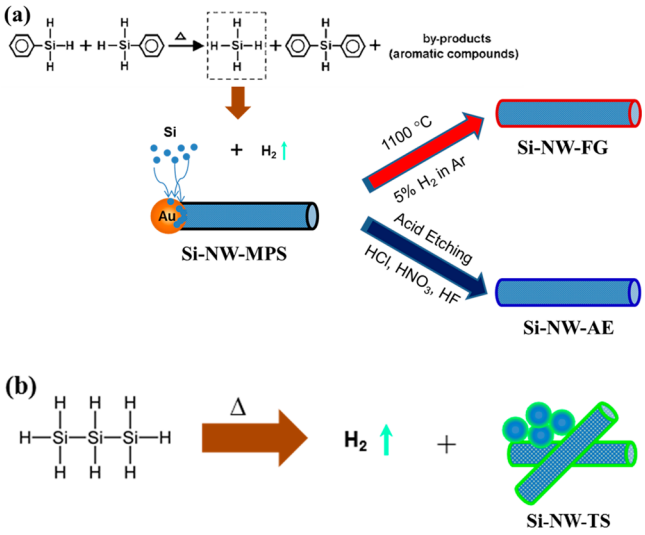

Figure 1. Schematic figures for the synthesis of the Si-NWs: (a) monophenylsilane (MPS) as the precursor and (b) trisilane (TS) as the precursor. The different edge color for different Si-NW samples indicates different surface functional groups.

(2) Si-NW-FG: Si nanowires produced in (1) above with annealing at 1100 °C in reducing atmosphere, forming gas i.e. 5% H_2 in Ar (FG).

(3) Si-NW-AE: Si nanowires produced in **1** were acid etched (AE) by first treating with it with aqua regia for 30 min followed by 30% HF.

(4) Si-NW-TS: Si nanowires synthesized with precursor trisilane (TS) where the Si:Au ratio is 45 and temperature of the reaction is 430 °C.

Electrochemical Evaluation and Materials Characterization. The electrochemical properties of these samples were evaluated in two-electrode coin-type cells (size 2032, Hohsen Corp.) on a Maccor multichannel battery tester (model 4000, Maccor Inc., Tulsa, OK) using pure lithium foil (99.9% pure, Alfa Aesar) as a counter electrode. The electrodes were prepared by manually pressing (approximately 20 psi) the Si-NW powders on Cu current collectors without the use of a binder or carbon black. The typical loading of the electrode was ∼0.1 mg/cm^2 with an electrode area of 1.0 cm^2. The electrolyte was 1.2 M $LiPF_6$ (lithium hexafluorophosphate) dissolved in a mixture of EC (ethylene carbonate) and DMC (dimethyl carbonate) (battery grade, Novolyte Technologies) in a volume ratio of 3:7 with HF and H_2O impurity levels of <50 and <5 ppm, respectively; a Celgard 2325 separator (Celgard Inc.) was used. The assembly of the coin cells was done in a high-purity argon-filled glovebox. The charge−discharge cycling (at 25 °C) was performed between 1.5 and 0.005 V with a current density of 200 mA/g.

X-ray photoelectron spectroscopy (XPS) was performed with a Thermo Scientific model K-Alpha XPS instrument. The instrument utilizes a monochromated, micro-focusing, Al Kα X-ray source (1486.6 eV) with a variable spot size (i.e., 30−400 μm). Analyses of the NWs samples were all conducted with a 400 μm X-ray spot size for the maximal signal magnitude and to obtain an average surface composition over the largest possible area. The instrument has a hemispherical electron energy analyzer equipped with a 128-channel detector system. The base pressure in the analysis chamber is typically ≤2 × 10^{-9} mbar. Samples were mounted on double-sided tape and introduced into the analysis chamber through a vacuum load-lock. Areas were chosen for analysis by viewing the samples with a digital optical camera with a magnification of approximately 60−200×. Survey spectra (0−1350 eV) were acquired for qualitative and quantitative analysis, and high-resolution spectra were acquired for appropriate elements for chemical state characterization. All spectra were acquired with the charge neutralization flood gun turned on to

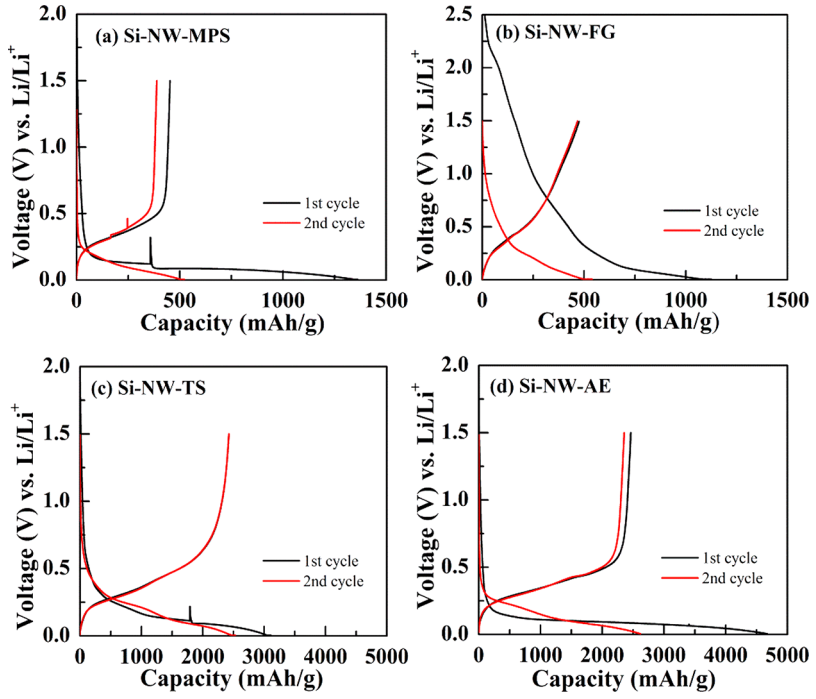

Figure 2. Galvanostatic voltage profile of the first two cycles for (a) Si-NW-MPS, (b) Si-NW-FG, (c) Si-NW-TS, and (d) Si-NW-AE.

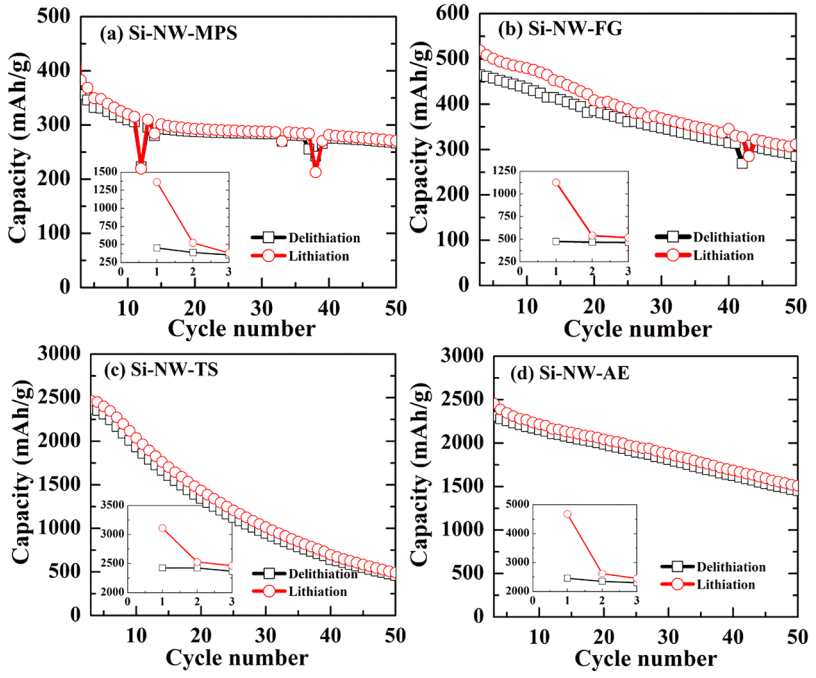

Figure 3. Cyclability of 50 cycles for (a) Si-NW-MPS, (b) Si-NW-FG, (c) Si-NW-TS, and (d) Si-NW-AE samples. The insets give the results of the first two cycles, and the following cycles 3−50 are shown in the main figures.

maintain stable analysis conditions on the nominally insulating oxide sample surface. The flood gun uses a combination of low-energy electrons and argon ions for optimal charge compensation. The typical pressure in the analysis chamber with the flood gun operating was 2×10^{-7} mbar. Data were collected and processed using the Thermo Scientific Advantage XPS software package (version 4.61). Peak fitting was performed using mixed Gaussian/Lorentzian peak shapes and a Shirley/Smart-type background. Depth profiling analyses were conducted with a Thermo Scientific EX06 argon-ion gun operated at 2000 eV and rastered over a 2 mm × 4 mm area. Sputtered depths were calibrated with a 100 nm SiO_2/Si standard.

Raman spectroscopy was performed using a WITec α-300 confocal microscope using a 532 nm excitation wavelength and a 50× microscope objective. The Raman signals were collected in the confocal geometry and dispersed through a spectrometer (600 lines/mm grating) and detected using a thermoelectric cooled CCD detector. Raman shifts were collected in the range of 100−3000 cm^{-1}. Transmission electron microscopy (TEM) was utilized to examine the morphology and size of the Si nanowires with the HF3300 S/TEM instrument, which was operated at 300 kV and equipped with a Bruker silicon drift EDS detector, which was used to obtain high-angle annular dark field (HAADF) STEM images and qualitative EDS maps.

dx.doi.org/10.1021/am500855a | ACS Appl. Mater. Interfaces 2014, 6, 7607−7614

RESULTS AND DISCUSSION

Electrochemical Performance of Pristine and Surface-Treated Si-NWs. The electrochemical performances of the four different Si-NW samples were evaluated at first by galvanostatic charge−discharge cycles. Figure 2 shows the charge−discharge voltage profiles for the first two cycles for all the samples described in Figure 1. The loading of the active material and the *C* rate are kept similar for all electrodes. The results are summarized briefly. (i) Si-NW-MPS and Si-NW-FG have much lower discharge capacities, in the range of 1000 mAh/g. (ii) The Si-NW-TS sample shows the best columbic efficiency for the first cycle. (iii) The Si-NW-AE sample shows the largest initial discharge capacity that is close to the theoretical capacity of Si (∼4000 mAh/g). The first discharge voltage profile of the Si-NW-FG sample (Figure 2b) has a capacity contribution at voltages much higher than 0.5 V, which could indicate some kind of irreversible redox reaction with the surface. It is expected that the dominant contribution to capacity is derived from the alloying reaction between Li and Si that generally occurs at potentials of ≤0.2 V.[12] However, from the second cycle onward, the voltage profile moves down to ≤1 V. The electrochemical performances of the four Si-NW samples are compared in Figure 3 by showing the charge−discharge capacity versus the number of cycles. Because silicon has a very high first-cycle irreversible capacity loss (ICL), the capacities of the first two cycles are shown in the inset. Although Si-NW-TS and Si-NW-AE samples have similar initial discharge capacities of ∼2500 mAh/g, we notice less capacity fade and/or loss for Si-NW-AE than for Si-NW-TS. At the end of cycle 50, Si-NW-AE still show discharge capacities on the order of 1500 mAh/g, while the values are <500 mAh/g for the Si-NW-TS. One of the hypotheses for such better capacity retention in the case of Si-NW-AE could be due the surface acid etching process that can potentially eliminate surface functionalities that are detrimental to electrochemical performance. It is also noteworthy to mention that the Si-NW-TS sample has a relatively high Au content (Si:Au ratio of 45) that could affect the electrochemical performance. Au is known to react with Li by forming alloys as reported in the literature.[33] These aspects will be discussed later in the following section.

Thus, distinct electrochemical performances are obtained for different batches of Si-NWs, synthesized from the same synthetic precursor with varying degrees of postprocessing conditions as described above. The correlation between the observed electrochemical performance of Si-NWs and their surface chemical functionalities was studied using different characterization techniques.

Correlation between Surface Chemistry and Electrochemical Properties. *Electron Microscopy Study of Si-NWs.* Transmission electron microscopy (TEM) was performed for these Si-NWs to evaluate morphologies in both bright-field and dark-field images as displayed in Figure 4. The remarkable feature is that the MPS sample displays a core−shell structure in which the shell is known to be composed of polyphenylsilane (Figure 4a,b).[32] A clear core−shell morphology was also observed for the FG sample (Figure 4c,d), which was obtained by annealing the Si-NW-MPS sample at 1100 °C under a reducing atmosphere. Such modification yields Si-NWs having an inner diameter in the range of 40 nm with an outer shell in the range of 10 nm. Chockla et al. reported that thermal annealing in forming gas can convert the phenylsilane shell to a carbonaceous layer comprising SiC.[32] For the Si-NW-TS sample, we notice both nanoparticles as well as nanowires (Figure 4e,f), in agreement with the results published previously.[31] The concomitant formation of nanoparticles along with NWs is due to the rapid decomposition of trisilane (TS) and homogeneous particle growth. In some NWs, Au NPs were found dispersed inside the Si-NWs and/or particles that may be caused by the rapid kinetics for the Si particle as well as the high percentage of Au NPs in the reagent. For the AE sample, it is clear that the acid etching removes the shell on the surface and leaves pristine Si-NWs with diameters ranging from 50 to 80 nm (Figure 4g,h).

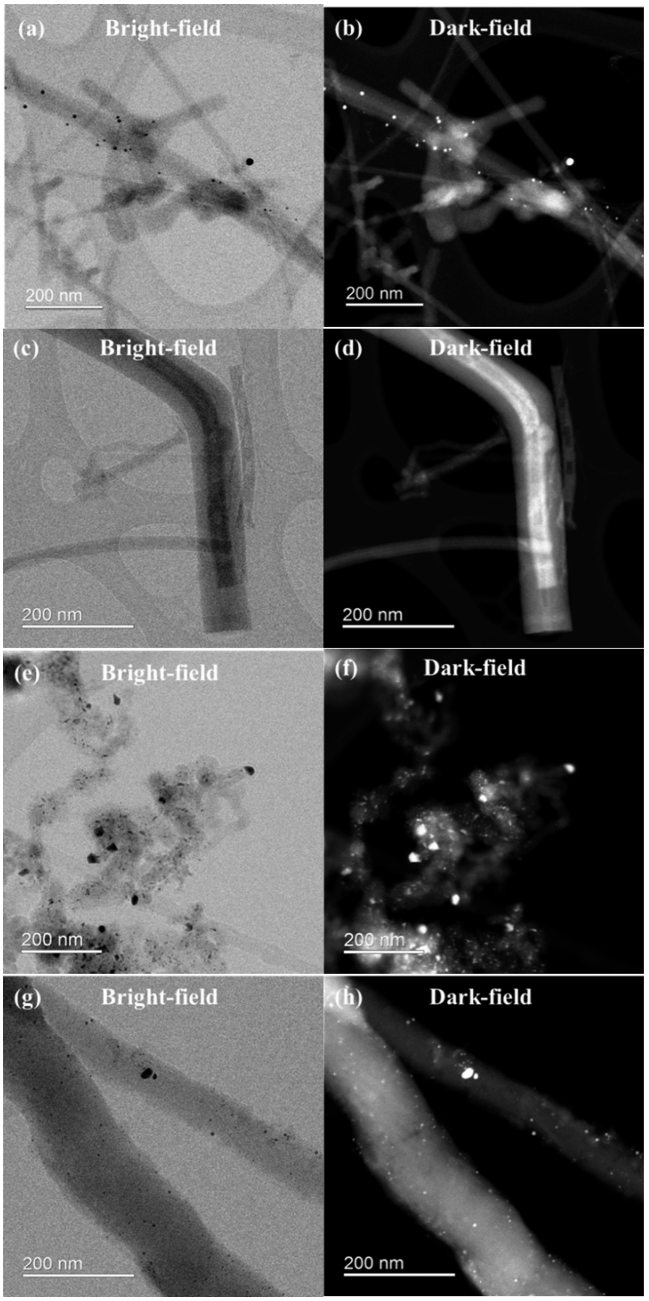

Figure 4. TEM images for Si-NW-MPS (a and b), Si-NW-FG (c and d), Si-NW-TS (e and f), and Si-NW-AE (g and h) samples.

Depth Profile X-ray Photoemission Spectroscopy of Si-NWs. X-ray photoelectron spectroscopy (XPS) combined with surface depth profiling was performed on various types of Si-NWs to evaluate their surface chemical composition. The

elemental concentrations of various species such as Si, O, C, and F are summarized in the histogram chart shown in Figure 5. A number of interesting conclusions can be derived from this analysis. In all forms of Si-NWs, we see varying degrees of silicon ranging from 25 to 45% and also significant coverage of carbon and oxygen. In some cases, the carbon and oxygen signal exceeds that of Si, indicating an outer shell that is either oxides or carbides of silicon (discussed below). The carbon XPS signal can arise from multiple factors, including the surface moieties present on Si-NWs, the underlying substrate (scotch tape), and adventitious carbon present in the XPS chamber. The small amount of F observed on the surface of the Si-NW-AE sample is attributed to HF etching. Traces of Au were also seen on the surface of TS and AE samples (not shown here), due to the residual Au NPs (see in TEM) from the synthesis process. To gain further insight into the different surface chemistries of each Si-NW sample, the C 1s, Si 2p, and, to a lesser extent, O 1s core level spectra were examined in detail. Figure 6 shows the C 1s, Si 2p, and O 1s core level spectra for each sample, after a brief *in situ* Ar-ion etching process (~30 s). The as-received samples showed varying amounts of inhomogeneous surface charging during acquisition of the core level spectra, in part because of the surface reactive nature of the samples (as described in the Supporting Information). The brief Ar-ion surface etching removed some of the surface-adsorbed and/or air-reacted outer material that also resulted in reducing the inhomogeneous charging that could shift and distort the XPS core level signal. In the data presented in Figure 6, the spectra have all been normalized to a fixed intensity to emphasize binding energy position and line shapes.

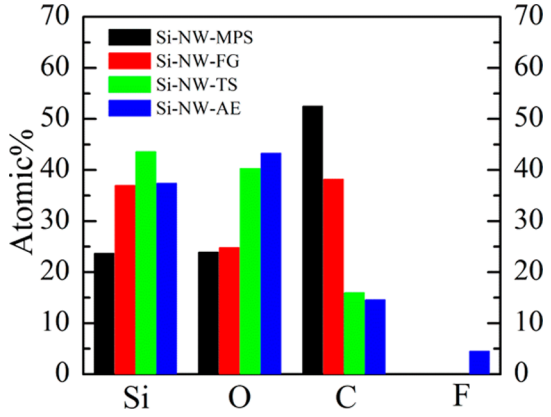

Figure 5. Atomic surface concentrations of elements Si, O, C, and F for Si-NW-MPS, Si-NW-FG, Si-NW-TS, and Si-NW-AE samples. The values were obtained from XPS survey scans (not shown here).

For C 1s, the Si-NW-MPS and Si-NW-FG samples show a large peak around ~283 eV that is attributed to C−Si bonding.[34] On the other hand, Si-NW-TS and Si-NW-AE samples have their surface chemistry dominated by C−C (and/or C−H) bonding, which is evident from the respective C 1s B.E value.[35] In addition, the Si-NW-FG sample also shows a significant peak intensity at the C−C B.E value. The Si 2p core level results are consistent with the observed C 1s core level where both Si-NW-MPS and Si-NW-FG show the expected Si−

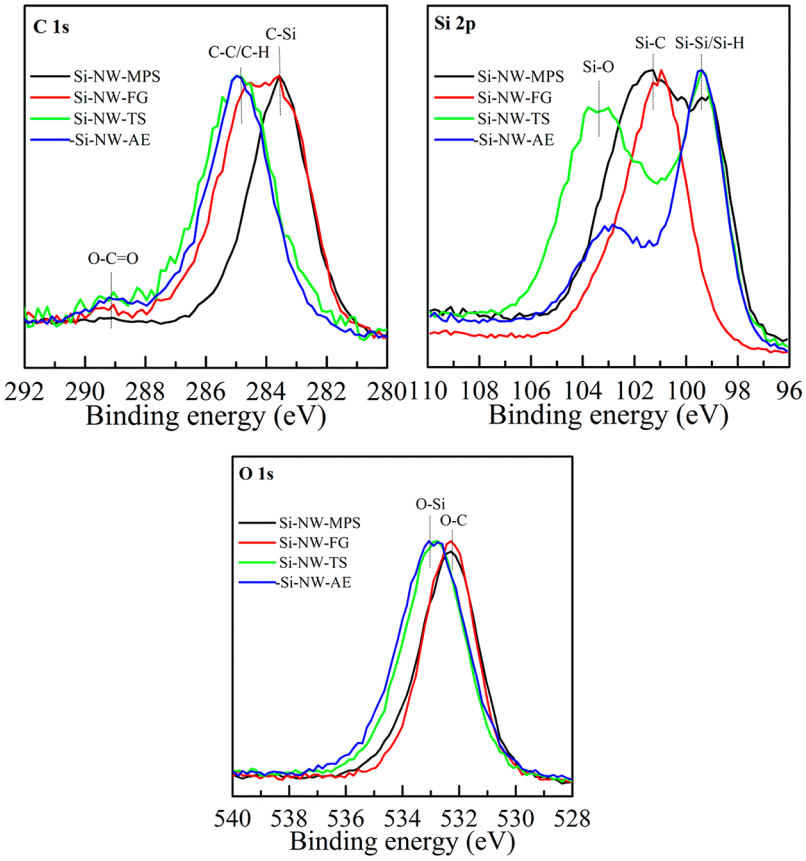

Figure 6. C 1s, Si 2p, and O 1s core level spectra for Si-NW-MPS (black), Si-NW-FG (red), Si-NW-TS (green), and Si-NW-AE (blue) samples. Bonding assignments are also shown.

dx.doi.org/10.1021/am500855a | ACS Appl. Mater. Interfaces 2014, 6, 7607−7614

C B.E values at ~101 eV.[36] In addition, the Si-NW-MPS also show significant coverage of Si−Si and/or Si−H moieties. For Si-NW-TS and AE samples, we see mainly the two components Si−Si/H and Si−O[36] with the oxide component significantly reduced for the acid-etched sample (Si-NW-AE). All Si-NW samples showed varying amounts of oxygen species as shown by the O 1s core levels, which could be mostly due to exposure to ambient conditions. The O 1s data show predominant Si−O bonding (predominantly SiO_2, but also could be some suboxides of silicon) for the Si-NW-TS and AE samples, consistent with the Si 2p data.[37] The Si-NW-FG and MPS samples show a relatively smaller Si−O feature with a predominantly O−C bonding environment, consistent with the C 1s core level. Suboxides refer to Si species with a valence below 4+, which generally can be described as SiO_x, where $1 < x < 2$.

The XPS analysis in conjunction with TEM results provides some degree of information about the various functional species that could exist on the surface of these Si-NWs. For the Si-NW-MPS sample, we most likely have an outer shell derived from MPS during the synthesis, which contributes to both Si−H and Si−C bonding. The Si-NW-FG samples are prepared by annealing at 1100 °C under forming gas; the monophenylsilane-derived shell can be converted more to a carbonaceous layer with both dominant C−C and Si−C surface groups. The outer shell for Si-NW-FG is much thicker in this case as shown in the TEM image (Figure 4c,d). For the Si-NW-TS sample, we do not expect any Si−C species as it is derived from the trisilane precursor, but as expected, it has a Si−O component due to the formation of a native oxide on the surface. The C 1s signal from Si-NW-TS most likely results from residual carbon from solvent decomposition and adventitious carbon present in the XPS chamber. For Si-NW-AE, we have a large fraction of exposed Si nanowires due to the etching process consistent with the TEM image shown Figure 4e,f. This explains the observation of a strong Si−Si XPS feature (99.4 eV) and also an unavoidable thin layer of SiO_x species formed on the surface of Si nanowires. We also expect the Si−H-terminated silicon surface for the Si-NW-AE sample, because of HF acid treatment, but this feature overlaps with the Si−Si B.E position.[38,39] X-ray synchrotron studies will undoubtedly shed more light on the depth dependence of various chemical moieties on these Si-NWs.[40]

Micro-Raman Study of Si-NWs. A Raman study further validates our XPS observations. As shown in Figure 7, all the samples show a peak at around 521 cm^{-1}, which is the first optical mode of Si.[32,41,42] The Raman peak intensities (under the same laser power and measurement conditions) vary for different Si-NWs, indicating the different chemical functionality of the Si-NWs. The strongest Si Raman band is observed for the Si-NW-AE sample, indicating that acid etching is helpful in removing the surface shell leading to pristine Si-NWs, while for the parent MPS-derived Si-NW, the Raman signal is weaker most likely because of the outer Si−C and Si−O shell. The presence of a large percentage of amorphous Si NPs in the TS sample could be another reason for the absence of a strong Raman peak for Si-NW-TS (apart from the surface shell). The most interesting case is the Si-NW-FG sample, which evidently has the weakest Si band but also two prominent bands at 1350 and 1600 cm^{-1}, corresponding to disordered (D) and graphitic (G) carbon, respectively.[43−46] This further corroborates the carbonization of the phenylsilane-derived shell during thermal annealing in the forming gas. Further, the Si-NW-FG sample has the thickest shell among all the Si-NWs (Figure 4). In addition to the main Si band at 521 cm^{-1}, another weak broad peak was also exhibited by MPS and AE samples, which can be assigned to the overtone of the TO(L) mode of Si.[41] The amorphous silicon signal (at ~480 cm^{-1}) originating from Si NPs for the Si-NW-TS sample was probably below the detection limit.

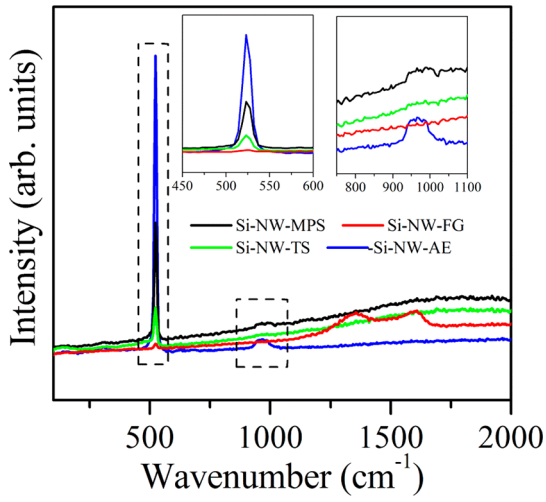

Figure 7. Raman spectra of Si-NW-MPS, Si-NW-FG, Si-NW-TS, and Si-NW-AE samples. The insets show expanded views of the dashed areas of the original spectra.

Correlation between Electrochemical Performance and Surface Functionality. On the basis of microscopy, XPS, and Raman results as discussed in the previous section, we provide a plausible explanation for the observed electrochemical performance for each Si-NW sample. A schematic picture showing the various surface groups that form the outer shell of the Si-NWs is shown in Figure 8. The monophenylsilane-derived shell on the surface of the Si-NW-MPS sample is detrimental to its electrochemical performance and cycle life. After being annealed in forming gas at 1100 °C, the phenylsilane-derived shell converts to a mixed carbon and SiC type of surface. The thick mixed layer of C and SiC covers the surface of the FG sample, hindering the access to the core Si-NW, especially because SiC is electronically insulating and electrochemically inactive. This explains their poor electrochemical performance

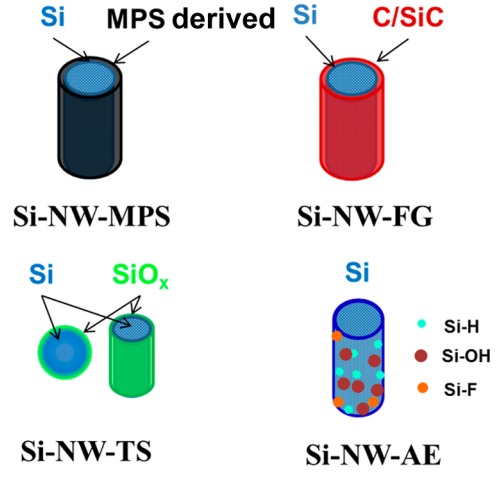

Figure 8. Surface chemical species present on the various kinds of Si-NW samples discussed in the text.

dx.doi.org/10.1021/am500855a | ACS Appl. Mater. Interfaces 2014, 6, 7607−7614

and different voltage profiles. For the trisilane-derived Si-NW-TS sample, the surface coverage is mostly oxides of silicon with no appreciable SiC or carbonaceous groups. A mixed proportion of Si-NWs and NPs (nanoparticles) with some gold impurities may not be an optimized materials system for good electrochemical capacity retention and cycle life. Overall, we realize better performance from the Si-NW-AE sample as the MPS-derived shell is etched by acid treatment, leading to relatively cleaner Si-NW surfaces for good capacity retention.

CONCLUSIONS

A series of Si-NWs have been synthesized by the SFLS growth method and characterized using electron microscopy, Raman spectroscopy, and XPS. Different precursors and processing steps (annealing and acid etching) brought different morphologies and surface functionalities for the Si-NWs, which contribute to their distinct electrochemical performance. It is plausible that different surface-terminating groups will form different SEI compositions, which could be the limiting factor for the cycle life.[39] For example, Si−H termination for the Si-NW-AE sample and Si−O for the Si-NW-TS sample would form different SEI compositions that could impact their cycle lives. The Si−OH and Si−H groups most likely would form a conductive SEI composition during the first-cycle electrochemical reduction with an electrolyte (mostly EC) compared to that of phenylsilane and SiC surface groups. Furthermore, Si−F species on the surface of the Si-NW-AE sample may be helpful in forming a more stable SEI layer. The presence of fluorine can shorten the length of oligomer chains present in the SEI layer, leading to a compact passivation film,[47] which is beneficial for the cycling life. On the basis of surface analysis, we have provided a mechanistic understanding of various chemical groups that form the shell of such NWs that could either enhance their electrochemical performance or be detrimental. More in-depth studies are required to gain additional insights regarding the role of surface functionality in SEI formation, composition, and stability for Si-NWs. This is quite challenging in the case of Si because of its enormous changes in volume during repeated electrochemical cycling that tend to re-form the SEI during each cycle. Nevertheless, our study probes the missing link between surface properties of different types of Si-NWs and their electrochemical performance that will eventually help to fabricate or tailor silicon surfaces at a molecular level for robust electrochemical activity.

ASSOCIATED CONTENT

Supporting Information

XPS mapping of the four Si-NW samples and comparison of surface elemental concentrations before and after aging in air. This material is available free of charge via the Internet at http://pubs.acs.org.

AUTHOR INFORMATION

Corresponding Authors

*E-mail: nandaj@ornl.gov.

*E-mail: yudhisthira.sahoo@emdmillipore.com.

Present Addresses

[§]Department of Chemistry, Indian Institute of Technology Hyderabad, Ordnance Factory Estate, Yeddumailaram, 502 205 Andhra Pradesh, India.

[⊥]Merck Chemicals Ltd., Chilworth Science Park, University Parkway, SO16 7QD Chilworth, UK.

[∥]Merck KGaA, Frankfurter Str. 250, 64293 Darmstadt, Germany.

Notes

The authors declare no competing financial interest.

ACKNOWLEDGMENTS

This research was performed at the Oak Ridge National Laboratory (ORNL) and sponsored by EMD-Millipore Inc. under the Material Science and Technology Division, Work-for Others (WFO) Program WF680901, and U.S. Department of Energy Agreement DE-AC05-00OR22725. The micro-Raman work was supported by the Assistant Secretary for Energy Efficiency and Renewable Energy, Office of Vehicle Technologies of the U.S. Department of Energy. EMD Chemicals is an affiliate of Merck KGaA, Germany.

REFERENCES

(1) Boukamp, B. A.; Lesh, G. C.; Huggins, R. A. All-Solid Lithium Electrodes with Mixed-Conductor Matrix. *J. Electrochem. Soc.* **1981**, *128*, 725−729.

(2) Misra, S.; Liu, N.; Nelson, J.; Hong, S. S.; Cui, Y.; Toney, M. F. In Situ X-ray Diffraction Studies of (De)lithiation Mechanism in Silicon Nanowire Anodes. *ACS Nano* **2012**, *6*, 5465−5473.

(3) Lee, D. J.; Lee, H.; Ryou, M.-H.; Han, G.-B.; Lee, J.-N.; Song, J.; Choi, J.; Cho, K. Y.; Lee, Y. M.; Park, J.-K. Electrospun Three-Dimensional Mesoporous Silicon Nanofibers as an Anode Material for High-Performance Lithium Secondary Batteries. *ACS Appl. Mater. Interfaces* **2013**, *5*, 12005−12010.

(4) Obrovac, M. N.; Krause, L. J. Reversible Cycling of Crystalline Silicon Powder. *J. Electrochem. Soc.* **2007**, *154*, A103−A108.

(5) Limthongkul, P.; Jang, Y.-I.; Dudney, N. J.; Chiang, Y.-M. Electrochemically-Driven Solid-state Amorphization in Lithium-Silicon Alloys and Implications for Lithium Storage. *Acta Mater.* **2003**, *51*, 1103−1113.

(6) Chan, C. K.; Peng, H.; Liu, G.; McIlwrath, K.; Zhang, X. F.; Huggins, R. A.; Cui, Y. High-performance Lithium Battery Anodes using Silicon Nanowires. *Nat. Nanotechnol.* **2008**, *3*, 31−35.

(7) Erk, C.; Brezesinski, T.; Sommer, H.; Schneider, R.; Janek, J. Toward Silicon Anodes for Next-Generation Lithium Ion Batteries: A Comparative Performance Study of Various Polymer Binders and Silicon Nanopowders. *ACS Appl. Mater. Interfaces* **2013**, *5*, 7299−7307.

(8) Li, J.; Dozier, A. K.; Li, Y.; Yang, F.; Cheng, Y.-T. Crack Pattern Formation in Thin Film Lithium-Ion Battery Electrodes. *J. Electrochem. Soc.* **2011**, *158*, A689−A694.

(9) Xu, Y. H.; Yin, G. P.; Zuo, P. J. Geometric and Electronic Studies of $Li_{15}Si_4$ for Silicon Anode. *Electrochim. Acta* **2008**, *54*, 341−345.

(10) Huggins, R. A. Lithium Alloy Negative Electrodes. *J. Power Sources* **1999**, *81*−*82*, 13−19.

(11) Martinez de la Hoz, J. M.; Leung, K.; Balbuena, P. B. Reduction Mechanisms of Ethylene Carbonate on Si Anodes of Lithium-Ion Batteries: Effects of Degree of Lithiation and Nature of Exposed Surface. *ACS Appl. Mater. Interfaces* **2013**, *5*, 13457−13465.

(12) Chan, C. K.; Ruffo, R.; Hong, S. S.; Cui, Y. Surface Chemistry and Morphology of the Solid Electrolyte Interphase on Silicon Nanowire Lithium-ion Battery Anodes. *J. Power Sources* **2009**, *189*, 1132−1140.

(13) Ruffo, R.; Hong, S. S.; Chan, C. K.; Huggins, R. A.; Cui, Y. Impedance Analysis of Silicon Nanowire Lithium Ion Battery Anodes. *J. Phys. Chem. C* **2009**, *113*, 11390−11398.

(14) Kasavajjula, U.; Wang, C.; Appleby, A. J. Nano- and Bulk-Silicon-based Insertion Anodes for Lithium-ion Secondary Cells. *J. Power Sources* **2007**, *163*, 1003−1039.

(15) Arico, A. S.; Bruce, P.; Scrosati, B.; Tarascon, J.-M.; van Schalkwijk, W. Nanostructured Materials for Advanced Energy Conversion and Storage Devices. *Nat. Mater.* **2005**, *4*, 366−377.

(16) Graetz, J.; Ahn, C. C.; Yazami, R.; Fultz, B. Highly Reversible Lithium Storage in Nanostructured Silicon. *Electrochem. Solid-State Lett.* **2003**, *6*, A194−A197.
(17) Szczech, J. R.; Jin, S. Nanostructured Silicon for High Capacity Lithium Battery Anodes. *Energy Environ. Sci.* **2011**, *4*, 56−72.
(18) Liu, H.; Li, Q. Enhanced Electrochemical Performance of Three-Dimensional Ni/Si Nanocable Arrays as a Li-Ion Battery Anode by Nitrogen Doping in the Si Shell. *ACS Appl. Mater. Interfaces* **2013**, *5*, 12190−12196.
(19) Ohara, S.; Suzuki, J.; Sekine, K.; Takamura, T. A Thin Film Silicon Anode for Li-ion Batteries Having a Very Large Specific Capacity and Long Cycle Life. *J. Power Sources* **2004**, *136*, 303−306.
(20) Cui, L.-F.; Ruffo, R.; Chan, C. K.; Peng, H.; Cui, Y. Crystalline-Amorphous Core−Shell Silicon Nanowires for High Capacity and High Current Battery Electrodes. *Nano Lett.* **2009**, *9*, 491−495.
(21) Song, T.; Xia, J.; Lee, J.-H.; Lee, D. H.; Kwon, M.-S.; Choi, J.-M.; Wu, J.; Doo, S. K.; Chang, H.; Park, W. I.; Zang, D. S.; Kim, H.; Huang, Y.; Hwang, K.-C.; Rogers, J. A.; Paik, U. Arrays of Sealed Silicon Nanotubes as Anodes for Lithium Ion Batteries. *Nano Lett.* **2010**, *10*, 1710−1716.
(22) Saint, J.; Morcrette, M.; Larcher, D.; Laffont, L.; Beattie, S.; Pérès, J. P.; Talaga, D.; Couzi, M.; Tarascon, J. M. Towards a Fundamental Understanding of the Improved Electrochemical Performance of Silicon−Carbon Composites. *Adv. Funct. Mater.* **2007**, *17*, 1765−1774.
(23) Kim, H.; Seo, M.; Park, M.-H.; Cho, J. A Critical Size of Silicon Nano-Anodes for Lithium Rechargeable Batteries. *Angew. Chem., Int. Ed.* **2010**, *49*, 2146−2149.
(24) Wang, B.; Li, X.; Luo, B.; Zhang, X.; Shang, Y.; Cao, A.; Zhi, L. Intertwined Network of Si/C Nanocables and Carbon Nanotubes as Lithium-Ion Battery Anodes. *ACS Appl. Mater. Interfaces* **2013**, *5*, 6467−6472.
(25) Jung, Y. S.; Lee, K. T.; Oh, S. M. Si−carbon Core−Shell Composite Anode in Lithium Secondary Batteries. *Electrochim. Acta* **2007**, *52*, 7061−7067.
(26) Choi, N.-S.; Yew, K. H.; Kim, H.; Kim, S.-S.; Choi, W.-U. Surface Layer Formed on Silicon Thin-film Electrode in Lithium Bis(oxalato) Borate-based Electrolyte. *J. Power Sources* **2007**, *172*, 404−409.
(27) Yen, Y.-C.; Chao, S.-C.; Wu, H.-C.; Wu, N.-L. Study on Solid-Electrolyte-Interphase of Si and C-Coated Si Electrodes in Lithium Cells. *J. Electrochem. Soc.* **2009**, *156*, A95−A102.
(28) Yuan, F.-W.; Yang, H.-J.; Tuan, H.-Y. Alkanethiol-Passivated Ge Nanowires as High-Performance Anode Materials for Lithium-Ion Batteries: The Role of Chemical Surface Functionalization. *ACS Nano* **2012**, *6*, 9932−9942.
(29) Magasinski, A.; Zdyrko, B.; Kovalenko, I.; Hertzberg, B.; Burtovyy, R.; Huebner, C. F.; Fuller, T. F.; Luzinov, I.; Yushin, G. Toward Efficient Binders for Li-Ion Battery Si-Based Anodes: Polyacrylic Acid. *ACS Appl. Mater. Interfaces* **2010**, *2*, 3004−3010.
(30) Holmes, J. D.; Johnston, K. P.; Doty, R. C.; Korgel, B. A. Control of Thickness and Orientation of Solution-Grown Silicon Nanowires. *Science* **2000**, *287*, 1471−1473.
(31) Lee, D. C.; Hanrath, T.; Korgel, B. A. The Role of Precursor-Decomposition Kinetics in Silicon-Nanowire Synthesis in Organic Solvents. *Angew. Chem., Int. Ed.* **2005**, *44*, 3573−3577.
(32) Chockla, A. M.; Harris, J. T.; Akhavan, V. A.; Bogart, T. D.; Holmberg, V. C.; Steinhagen, C.; Mullins, C. B.; Stevenson, K. J.; Korgel, B. A. Silicon Nanowire Fabric as a Lithium Ion Battery Electrode Material. *J. Am. Chem. Soc.* **2011**, *133*, 20914−20921.
(33) Taillades, G.; Benjelloun, N.; Sarradin, J.; Ribes, M. Metal-based Very Thin Film Anodes for Lithium Ion Microbatteries. *Solid State Ionics* **2002**, *152*−*153*, 119−124.
(34) Bhandavat, R.; Kuhn, W.; Mansfield, E.; Lehman, J.; Singh, G. Synthesis of Polymer-Derived Ceramic Si(B)CN-Carbon Nanotube Composite by Microwave-Induced Interfacial Polarization. *ACS Appl. Mater. Interfaces* **2012**, *4*, 11−16.
(35) Kanamura, K.; Shiraishi, S.; Takezawa, H.; Takehara, Z.-i. XPS Analysis of the Surface of a Carbon Electrode Intercalated by Lithium Ions. *Chem. Mater.* **1997**, *9*, 1797−1804.
(36) Ram, P.; Singh, J.; Ramamohan, T. R.; Venkatachalam, S.; Sundarsingh, V. P. Surface Properties of Electrodeposited α-Si:C:H:F Thin Films by X-ray Photoelectron Spectroscopy. *J. Mater. Sci.* **1997**, *32*, 6305−6310.
(37) Hollinger, G.; Himpsel, F. J. Probing the Transition Layer at The SiO_2-Si Interface using Core Level Photoemission. *Appl. Phys. Lett.* **1984**, *44*, 93−95.
(38) Ma, D. D. D.; Lee, C. S.; Au, F. C. K.; Tong, S. Y.; Lee, S. T. Small-Diameter Silicon Nanowire Surfaces. *Science* **2003**, *299*, 1874−1877.
(39) Xu, W.; Vegunta, S. S. S.; Flake, J. C. Surface-Modified Silicon Nanowire Anodes for Lithium-ion Batteries. *J. Power Sources* **2011**, *196*, 8583−8589.
(40) Sapra, S.; Nanda, J.; Pietryga, J. M.; Hollingsworth, J. A.; Sarma, D. D. Unraveling Internal Structures of Highly Luminescent PbSe Nanocrystallites Using Variable-Energy Synchrotron Radiation Photoelectron Spectroscopy. *J. Phys. Chem. B* **2006**, *110*, 15244−15250.
(41) Wang, R. P.; Zhou, G. W.; Liu, Y. L.; Pan, S. H.; Zhang, H. Z.; Yu, D. P.; Zhang, Z. Raman Spectral Study of Silicon Nanowires: High-order Scattering and Phonon Confinement Effects. *Phys. Rev. B* **2000**, *61*, 16827−16832.
(42) Nanda, J.; Datta, M. K.; Remillard, J. T.; O'Neill, A.; Kumta, P. N. In Situ Raman Microscopy during Discharge of a High Capacity Silicon−carbon Composite Li-ion Battery Negative Electrode. *Electrochem. Commun.* **2009**, *11*, 235−237.
(43) Kim, Y. A.; Fujisawa, K.; Muramatsu, H.; Hayashi, T.; Endo, M.; Fujimori, T.; Kaneko, K.; Terrones, M.; Behrends, J.; Eckmann, A.; Casiraghi, C.; Novoselov, K. S.; Saito, R.; Dresselhaus, M. S. Raman Spectroscopy of Boron-Doped Single-Layer Graphene. *ACS Nano* **2012**, *6*, 6293−6300.
(44) Tuinstra, F.; Koenig, J. L. Raman Spectrum of Graphite. *J. Chem. Phys.* **1970**, *53*, 1126−1130.
(45) Lespade, P.; Al-Jishi, R.; Dresselhaus, M. S. Model for Raman Scattering from Incompletely Graphitized Carbons. *Carbon* **1982**, *20*, 427−431.
(46) Nanda, J.; Remillard, J.; O'Neill, A.; Bernardi, D.; Ro, T.; Nietering, K. E.; Go, J.-Y.; Miller, T. J. Local State-of-Charge Mapping of Lithium-Ion Battery Electrodes. *Adv. Funct. Mater.* **2011**, *21*, 3282−3290.
(47) Abraham, D. P.; Furczon, M. M.; Kang, S. H.; Dees, D. W.; Jansen, A. N. Effect of Electrolyte Composition on Initial Cycling and Impedance Characteristics of Lithium-ion Cells. *J. Power Sources* **2008**, *180*, 612−620.